

Image-Guided Control of a Robot for Medical Ultrasound

Purang Abolmaesumi, *Student Member, IEEE*, Septimiu E. Salcudean, Wen-Hong Zhu, *Member, IEEE*, Mohammad Reza Sirouspour, *Student Member, IEEE*, and Simon P. DiMaio, *Student Member, IEEE*

Abstract—A robot-assisted system for medical diagnostic ultrasound has been developed by the authors. This paper presents the visual servo controller used in this system. While the ultrasound transducer is positioned by a robot, the operator, the robot controller, and an ultrasound image processor have shared control over its motion. Ultrasound image features that can be selected by the operator are recognized and tracked by a variety of techniques. Based on feature tracking, ultrasound image servoing in three axes has been incorporated in the interface and can be enabled to automatically compensate, through robot motions, unwanted motions in the plane of the ultrasound beam. The accuracy of the system is illustrated through a 3-D reconstruction of an ultrasound phantom. An Internet-based robot-assisted teleultrasound system has also been demonstrated.

Index Terms—3-D ultrasound, feature tracking, medical ultrasound robot, tele-ultrasound, ultrasound image servoing.

I. INTRODUCTION

MEDICAL ultrasound exams often require that ultrasound technicians hold the transducers in awkward positions for prolonged periods of time, sometimes exerting large forces. A number of studies indicate that sonographers suffer from an unusually high incidence of musculoskeletal disorders (e.g., [1]).

Motivated initially by the need to alleviate these problems and to present a more ergonomic interface to the ultrasound technicians, a teleoperation approach to diagnostic ultrasound has been proposed by the authors [2]–[4]. Fig. 1 shows the experimental setup. The system consists of a master hand controller, a slave manipulator that carries the ultrasound probe, and a computer control system that allows the operator to remotely position the ultrasound transducer relative to the patient's body. An inherently safe, light, backdrivable, counterbalanced robot has been designed and tested. The primary use envisaged for this robot is carotid artery examinations to diagnose occlusive disease in the left and right common carotid arteries — a major

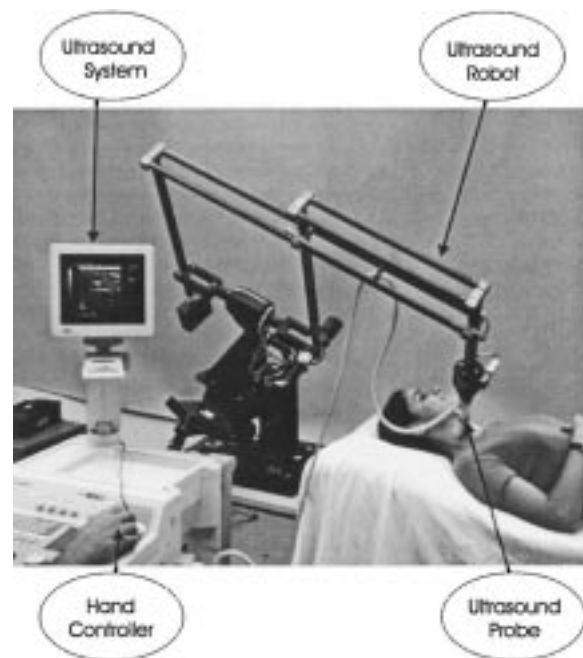


Fig. 1. Experimental setup for robot-assisted ultrasound. The 6-DOF parallelogram linkage robot moves the ultrasound probe on the patient's neck for the carotid artery examination.

cause of strokes [3]. The motion of the robot arm is based on measured positions and forces and acquired ultrasound images. The system uses a shared control approach that is capable of achieving motion, force and image control simultaneously.

The ability to interactively position the ultrasound probe via a teleoperated system, while being assisted with force and image controllers, has major advantages over other similar interfaces for ultrasound examination. In [5], [6], [7], a Mitsubishi PA-10 industrial robot was used with a force controller to assist ultrasound technicians to move the ultrasound probe against the patient's body. The ultrasound probe could only be moved by the robot, through a prespecified trajectory, which limits the flexibility of the examination. No shared control, teleoperation or ultrasound image servoing was reported. Other approaches, such as [8], [9], focus primarily on providing an interface for 3-D ultrasound image reconstruction.

In addition to having ergonomic benefits, the ability to remotely position the ultrasound probe could also be used in telemedicine. A number of interfaces for teleultrasound, such as [10], [11], require that an ultrasound technician be present at the examination site in order to manipulate the probe under the supervision of a remote radiologist, via real-time visual and

Manuscript received July 20, 2001. This paper was recommended for publication by Associate Editor J. Troccaz and Editor S. Hutchinson upon evaluation of the reviewers' comments. This work was supported by IRIS/PREARN Network of Centres of Excellence.

P. Abolmaesumi, S. E. Salcudean, M. R. Sirouspour, and S. P. DiMaio are with the Robotics and Control Laboratory, Department of Electrical and Computer Engineering, University of British Columbia, Vancouver, BC V6T 1Z4, Canada (e-mails: tims@ece.ubc.ca).

W. H. Zhu was with the Robotics and Control Laboratory, University of British Columbia, Vancouver, BC V6T 1Z4, Canada. He is now with Canadian Space Agency, 3A-220 Robotics Section, Spacecraft Engineering, Space Technologies, CSA, Agence Spatiale Canadienne, Saint-Hubert, QC J3Y 8Y9, Canada.

Publisher Item Identifier S 1042-296X(02)01777-9.

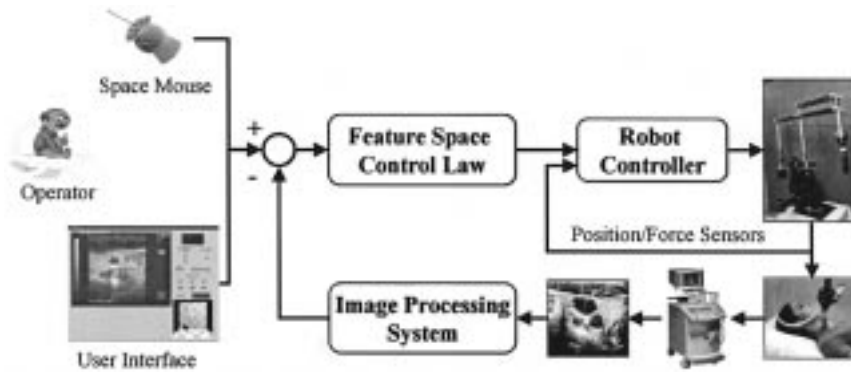


Fig. 2. Block diagram of the ultrasound robot system.

voice interaction. Robot-assisted teleultrasound examination have already been proposed in the literature [12]–[14], however none of the reported systems use a shared control approach to assist the operator in the teleultrasound examination. In contrast, our teleultrasound system allows the radiologist to view and manipulate the ultrasound transducer at the remote site by using a safe robot, while *being assisted* by the remote force and image servo controllers. The system has been demonstrated before [15].

The ability to automatically guide the ultrasound probe as a function of its acquired images, an approach termed “ultrasound image servoing”, could be a useful feature for diagnostic examinations when used in conjunction with human supervisory control, in order to reduce operator fatigue. During the ultrasound examination, the operator interacts with a graphical user interface and a hand controller. The resulting operator commands are coordinated with a local visual servoing system in order to control the robot, and thus the ultrasound-probe motion.

Several ultrasound image feature extraction and tracking algorithms have already been proposed in the literature [16], [17], [18], [19]. The real-time segmentation of medical images has been attempted before, especially in the context of cardiac echography [20], [21], [22], [23], with computation times of the order of seconds to tens of seconds per image frame being reported, unless specialized hardware is used [24], [25], [26]. Of particular interest to the problem of visual servoing and shared control is the ability to track images in real-time over a long period of time. Our own work on real-time feature extraction from ultrasound images has been reported in [3], [27], [28]. This paper summarizes these methods and compares their performance in carotid artery tracking. In addition, ultrasound image servoing to control three of the six degrees of freedom of a manipulator for robot assisted diagnostic ultrasound is demonstrated and some medical applications of the system are discussed.

The remainder of the of paper is organized as follows. Section II describes the system setup. Section III describes and compares the different feature extraction methods that have been developed to track the carotid artery in ultrasound images. Section IV presents the theory behind ultrasound image servoing, along with experimental results. Two applications of the system to the feature-based reconstruction of an ultrasound phantom in 3-D and to perform teleoperated ultrasound via the Internet are

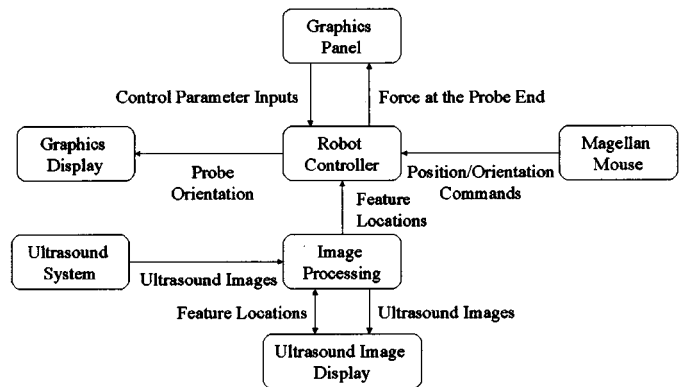


Fig. 3. Data flow in the system.

described in Section V. Finally, Section VI provides a summary and concluding remarks.

II. ROBOT ASSISTED MEDICAL ULTRASOUND

Fig. 2 shows the block-diagram of the experimental setup and Fig. 3 shows the inter-communication and data flow in the system.

The system consists of a slave manipulator carrying the ultrasound probe (see [3]), a user interface, and a computer control system.

A. The User Interface

The operator interacts with the system through the user interface, which consists of a master hand controller (a Space-Mouse™/Logitech Magellan™[29]) and a graphical user interface (GUI). The GUI was written using the gtk+ library under the Linux operating system. Fig. 4 shows a typical screen view of the GUI. It allows the operator to activate/deactivate the robot, to enable/disable the force control and the visual servoing and to enable/disable different degrees of freedom of the robot. Other features such as changing the sensitivity of the robot to the user positioning commands and switching the robot working frame from the world to the probe and vice versa are also incorporated in the GUI. The magnitude of the force applied to the patient is also displayed to the operator.

Ultrasound images are captured in real-time and are displayed in the GUI. A 3-D rendered model of the ultrasound transducer

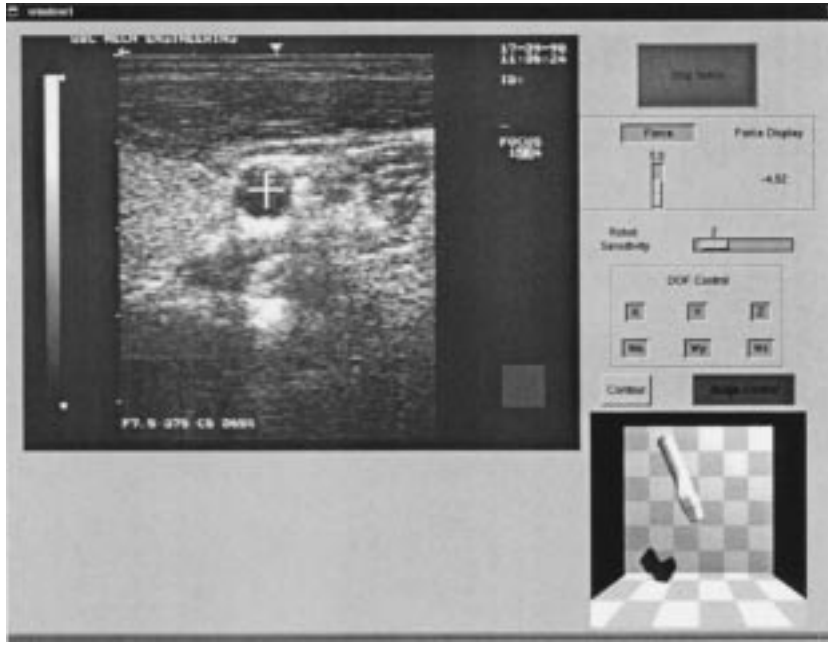


Fig. 4. Graphical user interface (GUI).

is also displayed. Ultrasound image features are selected by using the mouse. These features are passed to the image controller that compensates for motions in the plane of the ultrasound beam by moving the robot.

The velocity of all axes of the robot can be controlled by the SpaceMouse. All buttons and sliders in the GUI can be controlled by the keypad of the SpaceMouse.

B. Robot Controller

The control approach is explained in [30]. Its objective is to let a linear combination of the velocity and scaled force of the ultrasound probe track the hand controller command (its displacement from the nominal center). There is no explicit switching between the contact and free motion states. The controller uses the measured probe positions and forces, the acquired ultrasound images, and/or the commanded position and force trajectories simultaneously in a shared control approach to control the robot arm. The controller runs on a VxWorks™ real-time operating system.

Safety issues have been addressed in the design and control of the ultrasound robot and are discussed in [3]. Software limits have been used in the output of the image controller to limit the velocity command which is sent to the robot. In addition, the shared control feature of the robot allows the operator to guide the robot in the correct direction and to disable the image controller when the feature is lost.

III. FEATURE TRACKING IN ULTRASOUND IMAGES

Five feature tracking methods are presented here. These methods are the modified cross-correlation algorithm, the sequential similarity detection (SSD) algorithm, the Star algorithm, the Star-Kalman algorithm and the discrete snake algorithm. The image processing system captures the ultrasound images at a rate of 30 frames/s by using a Matrix Vision™ Mv-delta frame grabber and processes them at the same rate.



Fig. 5. A CAD model of the ultrasound phantom and the ultrasound transducer. The plane of the ultrasound beam which is emitted from the ultrasound transducer is also demonstrated.

An ultrasound phantom has been designed to test the performance of the feature tracking algorithms. Fig. 5 illustrates a CAD model of the phantom. Three plastic tubes are positioned in a solution [31] along three different axes in the phantom. An ultrasound image of the phantom is shown in Fig. 6, with the ultrasound transducer imaging plane being aligned with the xz -plane and pointing along the negative z -axis.

Experiments have been performed on the ultrasound phantom to quantitatively compare the effectiveness of the methods in tracking features in ultrasound images. In these experiments, the center of one of the pipes was selected as a feature in the ultrasound image and the robot was used to move the ultrasound probe back-and-forth with constant velocity along the x -axis of the probe coordinate frame. Figs. 6 and 7 show the concept.

The tracking of the carotid artery is also demonstrated on 10 second sequences of carotid artery images. The images are acquired when the ultrasound transducer is positioned and moved

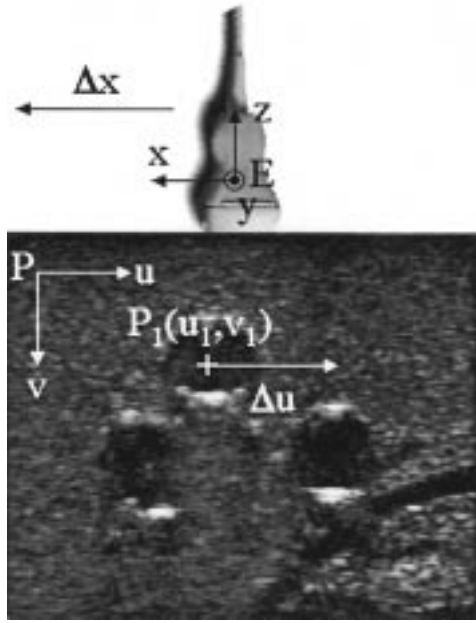


Fig. 6. An ultrasound image of the phantom. The figure shows the location of the ultrasound probe with respect to the ultrasound image. Any probe motion of Δx along the x -axis of the probe would cause a feature motion Δu along the u -axis of the image.

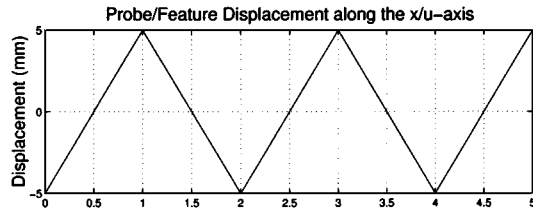


Fig. 7. Displacement of the probe along the x -axis (Δx) relative to the phantom; one pixel displacement in the ultrasound image along the u -axis corresponds to a motion of 0.123 mm of the robot end-effector along the x -axis.

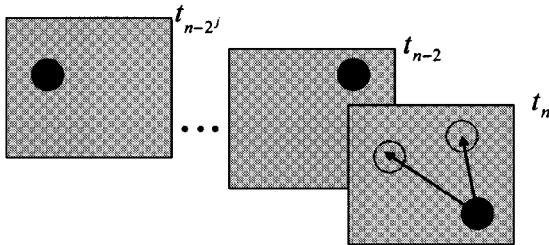


Fig. 8. A schematic diagram of the correlation algorithm.

on the neck of a patient by the sonographer. Real-time tracking results are shown in Figs. 10, 14 and 16.

A. Cross Correlation

The first approach evaluated for image tracking was the normalized cross-correlation technique [2]. In this method, a sub-block of the image acquired at time t_i is shifted in its neighborhood looking for a best correlated match with a fixed sub-block of the same size in a prior frame t_k . A schematic diagram of the algorithm is shown in Fig. 8. If k is fixed, the best correlation is sought relative to a fixed or reference image. Applying the cross-correlation method in this way leads to little drift, but high sensitivity to image deformation. If $i - k$ is fixed,

the best correlation is sought relative to an image acquired a fixed time offset relative to the current frame. Applying the cross-correlation method in this way leads to little sensitivity to image deformation, but to significant drift, as the shift estimate is being integrated. A mixed approach was implemented that seeks the best correlation relative to multiple frames at times $t_k, t_{k-2}, t_{k-4}, \dots, t_{k-2^n}$, where n is fixed. The feature point in this algorithm is defined as the center of the correlation window.

Fig. 9(a) shows the performance of the correlation algorithm with $n = 3$ for an image sub-block of 64×64 and Fig. 10 shows the tracking result for carotid artery images for an image sub-block of 64×64 .

B. Sequential Similarity Detection

A sequential similarity detection (SSD) [32] was implemented to track arbitrary features in ultrasound images. In this simple method of motion-energy detection, a sub-block of the image acquired at time t_i is shifted in its neighborhood looking for a minimum absolute subtraction (pixel by pixel) with a fixed sub-block of the same size in a prior frame t_k .

Fig. 9(b) shows the performance of the SSD algorithm for an image sub-block of 64×64 .

C. Star Algorithm

The Star algorithm [33] was implemented to track the carotid artery in real-time. The major advantage of this method is its robustness to cumulative error. The algorithm uses an edge-detection filter to detect the carotid artery boundary along rays emanating from a point interior to the carotid artery. It determines center coordinates of the cavity as the center of gravity of extracted boundary points. A schematic diagram of the method is shown in Fig. 11. Although the Star algorithm performs in real-time, it is relatively unstable [28], since the algorithm does not incorporate previous estimates of the carotid artery centroid. This can be improved by using a temporal Kalman filter.

Fig. 12 demonstrates the approach. A constant velocity kinematic model [34] is chosen for the motion of the carotid artery:

$$X(k+1) = \begin{bmatrix} 1 & T \\ 0 & 1 \end{bmatrix} X(k) + V(k) \quad (1)$$

$$Z(k) = [1 \quad 0] X(k) + \omega(k) \quad (2)$$

where $X(k) = [x(k) \quad \dot{x}(k)]^T$ is the system state (position and velocity of the carotid artery center), T is the sampling time of the system, $V(k)$ is the process noise vector with covariance $C(k)$, $Z(k)$ is the output of the Star algorithm, and $\omega(k)$ is its error with covariance $D(k)$. It is assumed that the acceleration can be modeled by zero-mean, white, Gaussian noise, and that the Star algorithm output is the noisy version of the actual position of the carotid artery. The recursive Kalman filter algorithm [34] is implemented to estimate the location of the center point of the carotid artery in consecutive ultrasound image frames.

Considering the range of probe velocities during an ultrasound examination, we chose $\sigma_v = 10$ pixel/s², where σ_v is the variance of the acceleration of a feature in the ultrasound image. With a sampling time of $T = .033$ s for a frame rate of 30 frames/s, we calculate $C(k) \approx \begin{bmatrix} 0.0 & 0.002 \\ 0.002 & 0.12 \end{bmatrix}$, and

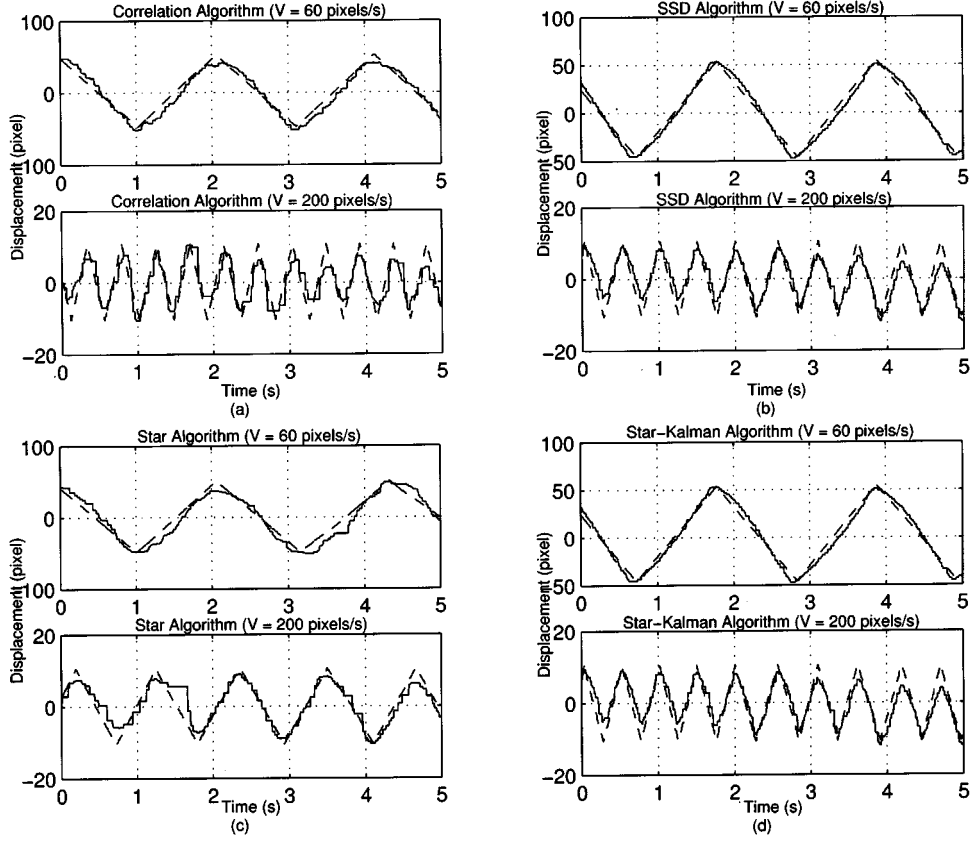


Fig. 9. The tracking performance of the feature tracking algorithms at two different velocities. In each figure, the dotted line shows the actual displacement of the feature and the continuous line shows the displacement of the extracted feature along the u -axis in the image.

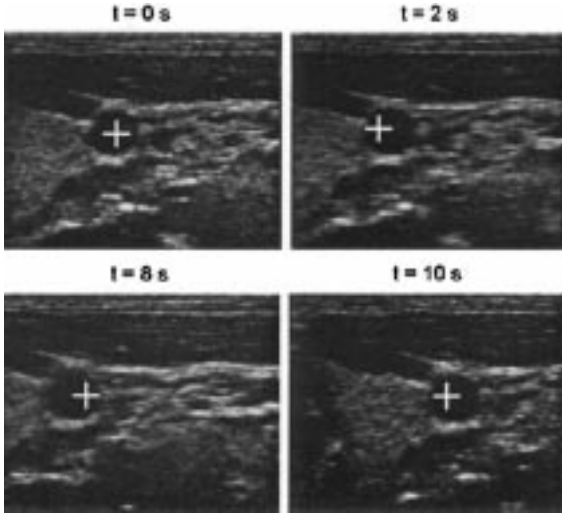


Fig. 10. Tracking the carotid artery by the correlation algorithm; the cross in the image shows the position of the feature.

$D(k) = 20$, for all k . Using these parameters, Fig. 9(c) shows the performance of the Star algorithm for different velocities of the ultrasound probe.

D. Star-Kalman Algorithm

This subsection describes the development of a novel fully automatic segmentation and tracking system to track the carotid artery in ultrasound images in real-time. The feature extraction

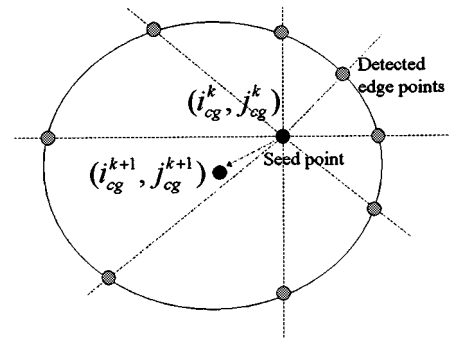


Fig. 11. Illustration of the Star algorithm; the central point is updated in each iteration as the center of gravity of the detected edge points.

method is inspired from [34], where the tracking of a single target in a randomly distributed cluttered environment is presented in the spatial domain. In each frame, N angularly equi-spaced radii are projected from $(\hat{i}_{cg}, \hat{j}_{cg})$, the center of gravity of the extracted contour points in the previous frame. The edge function used in the Star algorithm [33] is applied to all the pixels along each individual radius. Then, M points along each radius that have the highest edge function value are chosen.

Fig. 13 shows a schematic diagram of the method. Assuming a circular shape for the carotid artery, the following model could be used to describe the system:

$$d(k+1) = d(k) + \xi(k) \quad (3)$$

$$z(k) = d(k) + \phi(k) \quad (4)$$

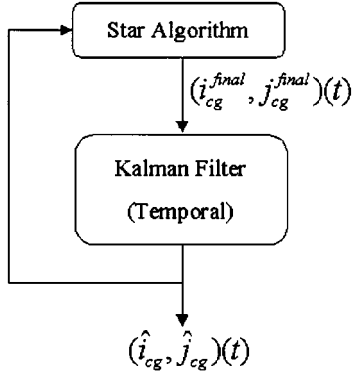


Fig. 12. Block diagram of the Star tracking method. $(i_{cg}^{final}, j_{cg}^{final})$ is the estimated position of the carotid artery using the Star algorithm. This information is used in a temporal Kalman filter to predict the location of the carotid artery $(\hat{i}_{cg}, \hat{j}_{cg})$ in the ultrasound image.

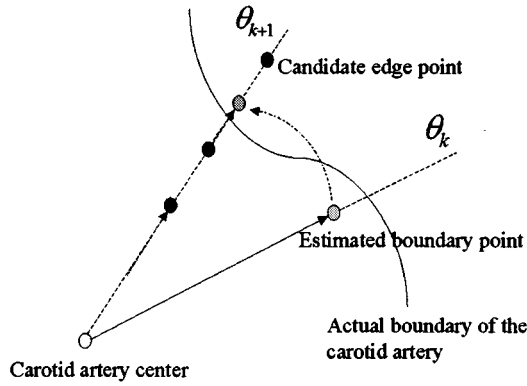


Fig. 13. A schematic diagram of the border extraction method; notations are described in the text.

where the state $d(k)$ is the radius of the boundary point along radius k . $z(k)$ is a noisy version of $d(k)$ (one of $r_i(k)$'s, where $r_i(k)$ is the distance of the i^{th} candidate edge point along radius k from the seed point, $i \in 1, 2, \dots, M$) at iteration k , and ξ and ϕ are sequences of zero-mean, white, Gaussian process and measurement noise values with covariances $Q(k)$ and $R(k)$, respectively. The curvature of the extracted feature can be determined by adjusting the values of $Q(k)$ and $R(k)$ with respect to each other.

Let the state of the filter $\hat{d}(k-1|k-1)$ at iteration $k-1$ be the radius of the estimated boundary point along radius $k-1$. The radius of the boundary can be estimated as

$$\hat{d}(k|k-1) = \hat{d}(k-1|k-1) \quad (5)$$

where the estimation of the boundary radius is updated using current radius candidate edge points as follows:

$$\hat{d}(k|k) = \hat{d}(k|k-1) + W(k)(z(k) - \hat{d}(k|k-1)) \quad (6)$$

where $W(k)$ is the Kalman filter gain. Since $z(k)$ is unknown, a combination of different candidate boundary points along radius k , $y(k)$, is used as measurement in the Kalman filter

$$y(k) = \sum_{i=1}^M r_i(k) \beta_i. \quad (7)$$

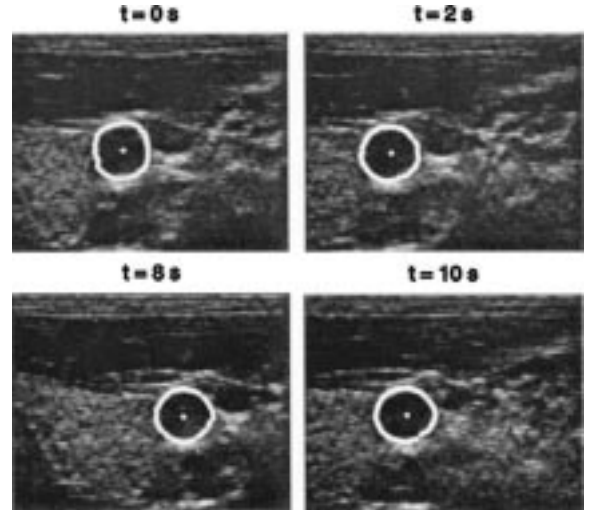


Fig. 14. Tracking the carotid artery by the Star-Kalman algorithm; the extracted carotid artery contours is shown in the image.

The β_i 's are weighting factors determined by the likelihood of each candidate edge point i on radius k being on the actual boundary. The β_i 's can be computed by assuming a normal distribution around the actual boundary for each estimated edge point. The edge magnitudes are also incorporated in the calculation of the β_i 's. Thus, the following formulation can be used to compute the β_i 's:

$$\beta_i(k) = \frac{p_i(k)}{\sum_i p_i(k)} \quad (8)$$

where

$$p_i(k) = \frac{F_{edge}(r_i(k), \theta_k)^2}{\sqrt{2\pi S(k)}} \exp \left(-\frac{(y(k) - \hat{d}(k|k-1))^2}{2S(k)} \right) \quad (9)$$

is the probability distribution function of the correct measurement, assuming that the distribution density of the candidate edge points around the real boundary point is normal. The function $F_{edge}(r_i(k), \theta_k)$ is the magnitude of the edge at the point $(r_i(k), \theta_k)$ in polar coordinates, $S(k)$ is the measurement prediction covariance, and $\hat{d}(k|k-1)$ is the predicted state of the system at iteration k . Note that the probability distribution in (9), p_i , is calculated such that an edge point with a higher edge magnitude has a higher probability to be the correct measurement.

Implementation results show excellent performance. Fig. 9(d) shows the performance of the Kalman algorithm for different velocities of the ultrasound probe. Fig. 14 shows the tracking result on the carotid artery images when $R(k) = 20$ and $Q(k) = 3$. $R(k)$ and $Q(k)$ are chosen based on trial and error to give an acceptable performance in tracking the carotid artery in ultrasound images.

E. The Discrete Snake Model

The snake model was originally proposed to find a continuous closed contour that minimizes an energy function. Snake models can be trapped by noise easily, and the weighting factors that control their deformation behavior are difficult to compute.

To solve these problems, we follow the approach proposed in [35]. Rather than performing snake deformation on the original image, the discrete snake model carries out energy minimization on selected edge points of the original image.

Instead of using an early vision model described in [35], a method similar to the Star algorithm to find candidate edge points has been used. In each frame, N angularly equispaced radii are projected from $(\hat{i}_{cg}, \hat{j}_{cg})$, the center of gravity of the extracted contour points in the previous frame. The edge function used in the Star algorithm is applied to all the pixels along each individual radius. Then, M points along each radius that have the highest edge function value are chosen as the candidate edge points. The following energy function is minimized among the candidate edge points to find the carotid artery contour [35]:

$$E_{snake}^K(i) = (\alpha^K(i)|\Gamma_s^K(i)|^2 + \beta^K(i)|\Gamma_{ss}^K(i)|^2) - 3I(v^K(i)) - \gamma^K(i) \int \int_R dA \quad (10)$$

The contour $\Gamma(s) = (x(s), y(s))$ is the parametric representation of the contour, where s is the arc length of the contour and $\Gamma_s(s)$ and $\Gamma_{ss}(s)$ are the absolute values of the first order derivative and the second order derivative, respectively. $\alpha^K(i) \geq 0$, $\beta^K(i)$ and $\gamma^K(i)$ show the weighting factors that control the stretching property, the bending property and the centrifugal force at the candidate edge point K along the i^{th} radius, respectively, $v^K(i)$ is the candidate edge point K along the i^{th} radius, $I(v)$ represents the intensity of the image at point v and $\int \int_R dA$ is the balloon force that is the area of the region R enclosed by the snake. To keep the internal force in balance with the image force, $\alpha^K(i)$, $\beta^K(i)$ and $\gamma^K(i)$ are chosen such that [35]:

$$\alpha^K(i) = \frac{I(v^{K-1}(i))}{|\Gamma_s^{K-1}(i)|^2} \quad (11)$$

$$\beta^K(i) = \frac{I(v^{K-1}(i))}{|\Gamma_{ss}^{K-1}(i)|^2} \quad (12)$$

$$\gamma^K(i) = \frac{I(v^{K-1}(i))}{\int \int_R dA} \quad (13)$$

where $I(v^{K-1}(i))$, $|\Gamma_s^{K-1}(i)|^2$, $|\Gamma_{ss}^{K-1}(i)|^2$ and $\int \int_R dA$ denote the image force, continuity force, curvature force and balloon force of the last iteration for each point on the contour respectively.

Fig. 15 shows the performance of the Snakes algorithm. As well, Fig. 16 shows the tracking result on the carotid artery images.

F. Discussion

Table I presents the error percentage of feature tracking algorithms for two different velocities. The data shows that both the SSD and the Star-Kalman algorithms can be used with a small error to track features in ultrasound images at different velocities. The Snake algorithm is the least reliable one, as the algorithm loses the feature and diverges after $V = 100$ pixels/s.

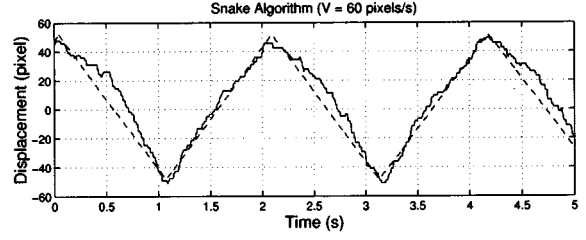


Fig. 15. The tracking performance of the Snakes algorithm at $V = 60$ pixels/s. The dotted line shows the actual displacement of the feature and the continuous line shows the displacement of the extracted feature along the u -axis in the image.

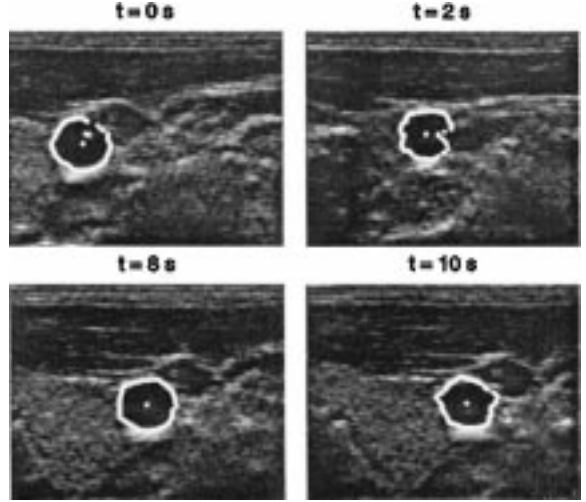


Fig. 16. Tracking the carotid artery by the snake algorithm; the extracted carotid artery contours is shown in the image.

TABLE I
COMPARISON OF DIFFERENT FEATURE TRACKING ALGORITHMS; S_{60} AND S_{200} REPRESENT STANDARD DEVIATIONS OF THE ERROR IN DESIRED FEATURE VELOCITIES OF 60 PIXELS/S AND 200 PIXELS/S, RESPECTIVELY AND R REPRESENTS THE PEAK TO PEAK DISPLACEMENT OF THE ACTUAL FEATURE ALONG THE u -AXIS IN PIXELS

Method	S_{60}/R	S_{200}/R	kflops/frame
Correlation	8.7%	15.5%	100
SSD	6.3%	13.5%	50
Star	10.7%	18.9%	30-150
Star-Kalman	6.5%	13.6%	20
Snakes	8.0%	N/A	50-300

IV. ULTRASOUND IMAGE SERVOING

One of the main features of the current system is its ability to visually track features in ultrasound images in real-time. This could help ultrasound technicians in guiding the motion of the ultrasound probe during the examination. The feature tracking algorithms provide the image controller with the required feature coordinates (e.g., the center of the carotid artery) to control the robot.

A. Image Servo Controller

The feasibility of the ultrasound image servoing to control three axes of the robot can be determined by examining the ultrasound image Jacobian, that relates differential changes in the

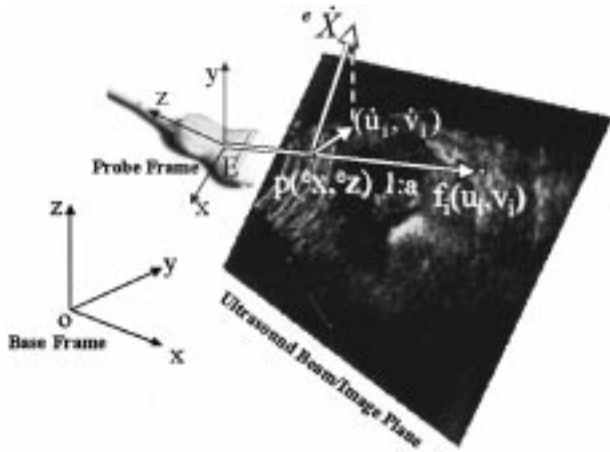


Fig. 17. Definition of the frames for the ultrasound robot.

image features to differential changes in the configuration of the robot. Fig. 17 illustrates the concept.

Let $f_i = [u_i, v_i]^T$ be a feature point in the ultrasound image plane coinciding with a point p with coordinates ${}^e p = [{}^e x, {}^e y, {}^e z]^T$ in the probe-attached frame. The following relation holds

$${}^o p = {}^o d_e + {}^o C_e {}^e p \quad (14)$$

where the entries of ${}^o p$ are the coordinates of p in the base coordinate frame, the entries of ${}^o d_e$ are the end-effector coordinates in the base frame and the columns of ${}^o C_e$ are the coordinates of the end-effector frame with respect to the base frame. Suppose that the point p does not move, i.e., ${}^o \dot{p} = 0$. Taking the time derivative of (14), we have

$${}^e \dot{p} = -{}^o C_e^T {}^o \dot{d}_e + ({}^e p \times) {}^o C_e^T {}^o \omega_e \quad (15)$$

or

$${}^e \dot{p} = [-I | ({}^e p \times)] \begin{bmatrix} {}^e \dot{d}_e \\ {}^e \omega_e \end{bmatrix} \quad (16)$$

where

$$\begin{bmatrix} x \\ y \\ z \end{bmatrix} \times = \begin{bmatrix} 0 & -z & y \\ z & 0 & -x \\ -y & x & 0 \end{bmatrix} \quad (17)$$

Assuming an orthographic projection model [36] with scale a for the ultrasound image and that p remains in the image plane, the coordinates of f_i in the two-dimensional ultrasound image become $[u_i - u_0, 0, v_i]^T = [a {}^e x, 0, a {}^e z]^T$ (Fig. 17), where $[u_0, v_0]^T$ are the center coordinates of the ultrasound image with respect to the image frame. Thus from (16), we obtain that

$$\dot{f}_i = \begin{bmatrix} \dot{u}_i \\ \dot{v}_i \end{bmatrix} = \begin{bmatrix} a & 0 & 0 & 0 & -v_i & 0 \\ 0 & 0 & a & 0 & u_i - u_0 & 0 \end{bmatrix} \begin{bmatrix} {}^e \dot{d}_e \\ {}^e \omega_e \end{bmatrix} = J {}^e \dot{X} \quad (18)$$

where ${}^e \dot{X}$ are the translational and angular end-effector velocities in end-effector coordinates and $J \in \mathbb{R}^{2 \times 6}$ is the ultrasound image Jacobian matrix. If m feature points are considered in the image, similar pairs of rows will be added to (18):

$$\dot{f}_{2m \times 1} = J_{2m \times 6} {}^e \dot{X} \quad (19)$$

The column rank of the resulting Jacobian is at most three. Two or more feature points will generate a Jacobian of rank three. Thus, as expected, with nontrivial ultrasound images, it is possible to control the motion of the ultrasound transducer in three degrees of freedom in its image plane.

We have considered so far a simple proportional controller shown in Fig. 18

$${}^e \dot{X}_d = -J^\dagger [K_d (f_i - f_r) - \dot{f}_r], \quad (20)$$

where $f_i = [u_i, v_i]^T$ is the actual image feature location in the ultrasound image f_r is its desired location J^\dagger is the pseudo-inverse of J , $K_d = k_d I_{2m \times 2m}$ is the controller gain ${}^e \dot{X}_d$ is the commanded robot velocity.

B. Stability Analysis

Two cases will be considered in the visual servoing stability analysis, depending on the number of features tracked in the image. In the following analysis, it is assumed that the dynamics of the robot control loop are negligible relative to the image control loop, i.e., ${}^e \dot{X}_d = {}^e \dot{X}$.

1) *Tracking One Feature in the Ultrasound Image:* In this case, ${}^e \dot{X}$ is the minimum norm solution of (18), with J^\dagger given by

$$J^\dagger = J^T (J J^T)^{-1} \quad (21)$$

Replacing ${}^e \dot{X} = {}^e \dot{X}_d$ from (20) in (18) and using (21), the following equation is derived:

$$\dot{e}(f) + k_d e(f) = 0 \quad (22)$$

where $e(f) = f_i - f_r$. This guarantees that the tracking error converges to zero provided that $k_d > 0$.

2) *Tracking Two or More Features in the Ultrasound Image:* In this case, ${}^e \dot{X}^c$ is the least squares solution of (19) and J^\dagger is given by

$$J^\dagger = (J^c T J^c)^{-1} J^c T \quad (23)$$

where $J^c \in \mathbb{R}^{2m \times 3}$ and ${}^e \dot{X}^c \in \mathbb{R}^{3 \times 1}$ are defined as

$$\begin{bmatrix} \dot{u}_1 \\ \dot{v}_1 \\ \vdots \\ \dot{u}_m \\ \dot{v}_m \end{bmatrix} = \begin{bmatrix} a & 0 & -v_1 \\ 0 & a & u_1 - u_0 \\ \vdots & \vdots & \vdots \\ a & 0 & -v_m \\ 0 & a & u_m - u_0 \end{bmatrix} \begin{bmatrix} {}^e \dot{d}_{e_x} \\ {}^e \dot{d}_{e_z} \\ {}^e \omega_{e_y} \end{bmatrix} = J^c {}^e \dot{X}^c \quad (24)$$

We assume that any feature vector in the image plane can be written as follows:

$$f = f^c + f^n \quad (25)$$

where f^c and f^n lie in the range space and null space of $J^c T$, respectively. It can be shown that:

$$J^c J^\dagger = I - \sum_{i=4}^{2m} b_i b_i^T \quad (26)$$

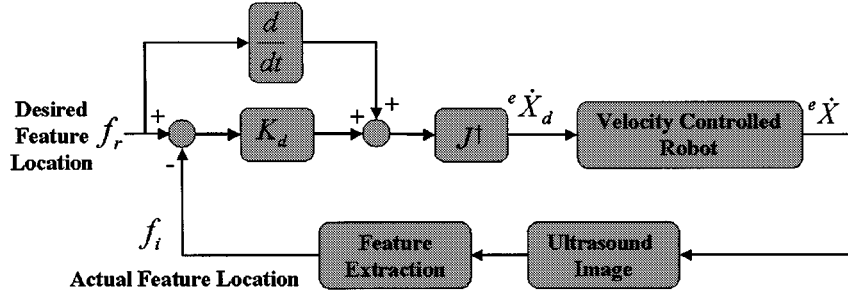


Fig. 18. Ultrasound image controller.

where the b_i 's are orthogonal basis vectors for J^T . Using (20), (23), (24) and (26), we have

$$\dot{f}_i^c + \dot{f}_i^n = -k_d (f_i^c - f_r^c) + \dot{f}_r^c \quad (27)$$

If we define the error vector $e(f^c) = f_i^c - f_r^c$, equation (27) can be written as

$$\dot{e}(f^c) + k_d e(f^c) + \dot{f}_i^n = 0 \quad (28)$$

Since $e(f^c)$ and \dot{f}_i^n belong to two orthogonal spaces, we have

$$\begin{aligned} \dot{e}(f^c) + k_d e(f^c) &= 0 \\ \dot{f}_i^n &= 0 \end{aligned} \quad (29)$$

which guarantees that image feature servoing

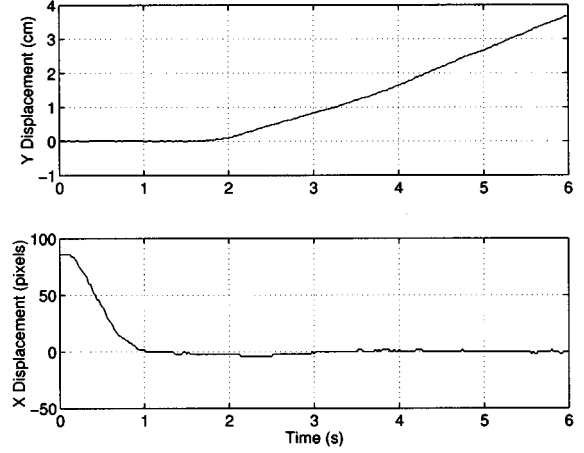
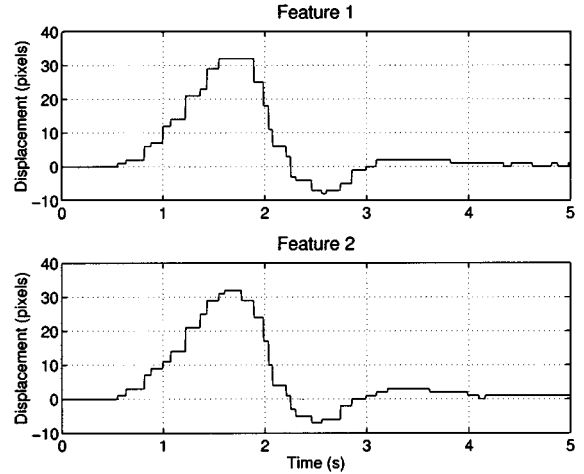
$$(f_i^c) \longrightarrow (f_r^c) \quad (30)$$

is achieved when $k_d > 0$. From (29), \dot{f}_i^n is constant, meaning that certain desired feature locations cannot be achieved by the image servo controller. From (18), it can be shown that the distance between every two feature points in the image is preserved while the features are moved in the ultrasound image.

C. Experimental Results

Ultrasound image servoing at rates as high as 30 Hz has been achieved to control up to three axes of the robot, while tracking one or two features (e.g., center of the pipes in Fig. 6) in the ultrasound image. With the coordinate system illustrated in Fig. 17, the control axes are the translations along the x -axis and z -axis, while the rotation is about the y -axis. In all the experiments, force control was disabled. Fig. 19 shows the ultrasound image servoing performance for one of the axes. For this experiment, a feature (center of one of the pipes in the phantom ultrasound image) is selected before enabling the visual servoing. While the operator is moving the probe along the y axis, the feature position is maintained in the center of the image automatically. The Star-Kalman algorithm [28] is used to extract the feature from the ultrasound image.

The performance of the system while tracking two features (center of two pipes in the phantom ultrasound image) simultaneously is shown in Fig. 20. Three degrees of freedom of the robot are controlled by the image servo controller in this experiment. The two features are moved away from their reference


 Fig. 19. Experimental results for image servoing in a single axis. The position of one feature is maintained in the center of the image (bottom figure) while the robot is displaced along y -axis (top figure).

 Fig. 20. Experimental results for image servoing in three axes; the position of the two features along the u -axis are changed by 30 pixels.

points at $t = 0.7$ s by moving the robot along the x -axis and are moved back by the image servoing action. In this experiment, $K_d = I_{4 \times 4}$ Hz.

We report ultrasound image servoing results using the phantom because the results are quantifiable and repeatable. The ultrasound image servoing has been tested in tracking the carotid artery in a number of volunteers in our laboratory and was found to work very well.

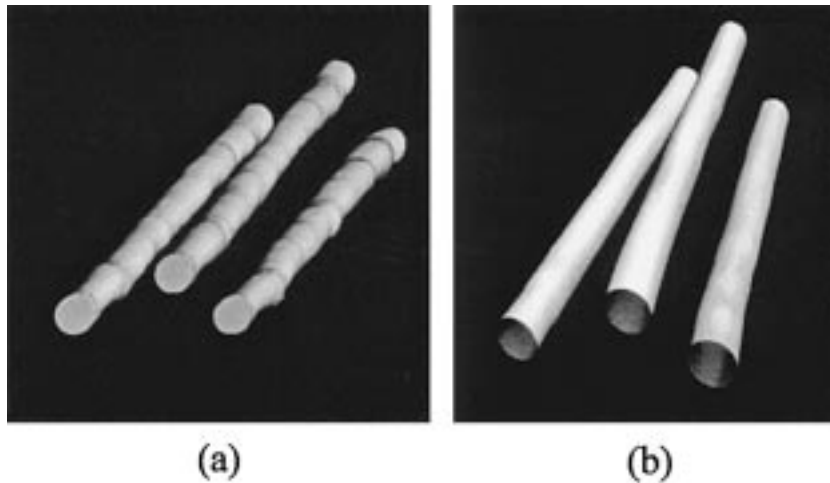


Fig. 21. Partial 3-D image reconstruction of the ultrasound phantom by using: a) the Stradx program, b) the Star-Kalman contour extraction method.

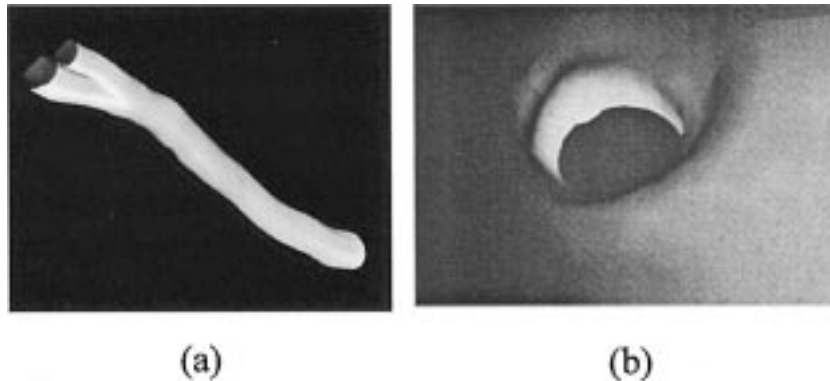


Fig. 22. Carotid artery 3-D reconstruction. (a) External view. (b) Internal view.

V. PRACTICAL APPLICATIONS

A. 3-D Ultrasound Imaging

Since the location of the ultrasound transducer can be determined via the forward kinematics of the slave manipulator, three-dimensional ultrasound images can be reconstructed from a series of two-dimensional image slices. While this can be achieved with any position/orientation tracker of the ultrasound probe, the feature detection algorithms presented in this paper allow real-time geometric model building with very little storage or computational overhead. For example, a vascular model could be built while the transducer is scanning arteries or veins to provide the ultrasound technician with a 3-D model for reference and guidance. The ultrasound phantom was used in this experiment to demonstrate the accuracy of the 3-D ultrasound imaging. A calibration method similar to the “three-wire” technique [37] was used to calibrate the system. This section discusses the two different 3-D reconstruction methods that have been implemented. Similar results have been obtained from carotid artery scans.

1) *Stradx*: Stradx [38] is a tool for the acquisition and visualization of 3-D ultrasound images using a conventional 2D ultrasound machine and an Ascension Bird™ position sensor. The contours that specify an anatomic region of interest are drawn in a series of two-dimensional image slices by the operator. These contours are mapped to a 3-D space by using the position in-

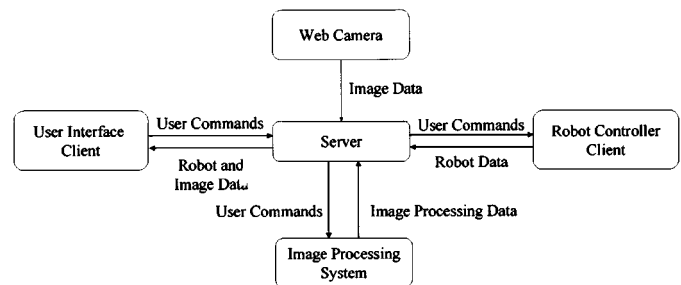


Fig. 23. Teleultrasound system setup.

formation provided by the sensor. In this application, the measured robot/probe position was substituted in place of the sensor data as input to the Stradx program. Since the resolution of the robot is higher than that of the Bird sensor and since it is independent of metal in the surrounding environment, the system provides a powerful tool for accurate 3-D reconstruction of ultrasound images. The Star-Kalman algorithm was used in each image to provide the Stradx software with the required segmentation data. Fig. 21 shows the 3-D reconstruction of the ultrasound phantom using this approach.

2) *Star-Kalman Based Reconstruction*: By using the Star-Kalman algorithm [27] to extract each pipe’s contour in the ultrasound image and the inverse kinematics of the robot to map each contour to the world coordinates, a 3-D image of each pipe

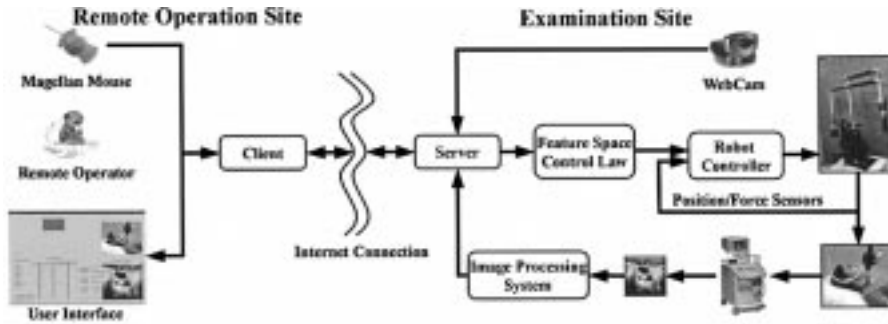


Fig. 24. Data flow in the teleultrasound system.

is reconstructed. Fig. 21 shows a partially reconstructed image. The reconstructed image has an average absolute error of less than 0.7 mm.

Fig. 22 shows two view points of a reconstructed 3-D image of the carotid artery by using the Star-Kalman reconstruction method. The robot was used to move the ultrasound probe along the neck of a volunteer subject. The Star-Kalman algorithm was used to extract the contours of the carotid artery. The figure clearly shows the shape and the bifurcation of the artery.

In contrast to the Stradx reconstruction approach, where the operator has to specify the contour of the desired region in each ultrasound image frame separately, this method extracts each pipe's contour automatically. The data storage requirements are much lower than that of the Stradx approach, as only the contour coordinates, and not the entire ultrasound images, are stored for 3-D reconstruction.

B. Teleultrasound

An application of the system as a teleultrasound device through the Internet is presented here. Fig. 23 shows the architecture of the experimental setup. A client-server application was written for this purpose under the Linux/Debian operating system. The server is responsible for relaying data between the user interface, the image processing system, the robot controller and the video camera. The server uses a JPEG compression algorithm to transfer ultrasound images to the remote operation site over a limited bandwidth. This could be improved by using an MPEG video compression method, which is not included in the current implementation of the system. At the same time, different operator commands are sent from the remote operation site to the server through this application. Fig. 24 shows the data flow in this application.

Two cameras send live video images, from two different viewing angles, to the operator from the examination site to the remote operation site through the client-server application. These images provide visual feedback for the operator to perform the ultrasound examination.

The system was demonstrated for the first time during the IRIS/PRECARN 2000 conference in Montreal. While the robot was located at the Robotics and Control Laboratory of the University of British Columbia (UBC) in Vancouver, conference delegates could interact with the user interface and the live visual feedback to successfully perform the ultrasound examination on an ultrasound phantom remotely.

While scalable to communication networks of almost any transmission speed, the demonstration was performed using a small portion of a shared 1.5 Mbit/s T-1 line at the conference center. With this transmission speed, a frame rate of at least 10 frames/s was achieved for ultrasound images and frame rates of 3 and 10 frames/s for the two cameras were achieved for the live video feedback. The ultrasound images had a resolution of 256×256 with an 8-bit gray scale. A visual feedback delay of approximately 500 ms was observed during the demonstration, because of the Internet transmission delay.

VI. SUMMARY AND CONCLUSIONS

Several real-time feature extraction and tracking algorithms have been developed. These methods have been compared for carotid artery tracking in ultrasound images. The Sequential Similarity Detection method and the Star-Kalman algorithm have been demonstrated to have excellent performance while tracking features with motions of up to 200 pixel/s; however, the Star-Kalman algorithm requires less computation time. The Correlation and Star algorithms exhibit poorer performance, with higher computational cost. The Snake algorithm was unable to track features with motions faster than 100 pixels/s.

These feature extraction methods are used in a medical ultrasound examination system that employs a robot to remotely position the ultrasound probe. An ultrasound image servoing capability is embedded in the system. Ultrasound visual servoing to control three axes of the robot has been demonstrated. The visual controller could help ultrasound technicians in guiding the motion of the ultrasound probe during the examination by maintaining a desired feature in the center of the ultrasound image. Two applications of the system in 3-D ultrasound image reconstruction and teleultrasound have also been described. Other potential applications of the system are image guided interventions, repeatable scanning and registration with images obtained with other imaging methods (e.g., MRI). The visual tracking algorithms could also be used to extract anatomical maps in real-time, which could help an ultrasound technician to guide the probe during an ultrasound examination.

In the future, the passive mouse will be replaced by a Power-Mouse haptic interface [39], in order to realize bilateral teleoperation with force feedback. Also, the system will be tested for diagnostic ultrasound at a Vancouver Hospital. A human factors study to compare the presented approach with that of the conventional ultrasound examination is also under way.

ACKNOWLEDGMENT

The authors wish to acknowledge the valuable assistance provided by research engineers S. Bachmann, R. Six, and H. Wong, by Prof. D. Lowe, and the ultrasound technicians at the Vancouver General Hospital, University of British Columbia, Vancouver, Canada.

REFERENCES

- [1] H. E. Vanderpool, E. A. Friis, B. S. Smith, and K. L. Harms, "Prevalence of carpal tunnel syndrome and other work-related musculoskeletal problems in cardiac sonographers," *J. Occup. Environ. Medicine*, vol. 35, no. 3, pp. 604–610, June 1997.
- [2] S. E. Salcudean, G. Bell, S. Bachmann, W. H. Zhu, P. Abolmaesumi, and P. D. Lawrence, "Robot-assisted diagnostic ultrasound — Design and feasibility experiments," in *Medical Image Computing and Computer Assisted Intervention*, C. Taylor and A. Colchester, Eds. New York: Springer, 1999, pp. 1062–1071.
- [3] S. E. Salcudean, W. H. Zhu, P. Abolmaesumi, S. Bachmann, and P. D. Lawrence, "A robot system for medical ultrasound," in *Robotics Research, the 9th Int. Symp. (ISRR'99)*, J. M. Hollerbach and D. E. Koditschek, Eds., 2000, pp. 195–202.
- [4] P. Abolmaesumi, S. E. Salcudean, W. H. Zhu, S. P. DiMaio, and M. R. Sirouspour, "A user interface for robot-assisted diagnostic ultrasound," in *IEEE Int. Conf. Robot. Auto.*, Seoul, South Korea, May 2001, pp. 1549–1554.
- [5] F. Pierrot, E. Domre, and E. Degoulange, "Hippocrate: A safe robot arm for medical applications with force feedback," *Med. Image Anal.*, vol. 3, pp. 285–300, 1999.
- [6] E. Degoulange, S. Boudet, J. Gariepy, F. Pierrot, L. Urbain, J. L. Megnien, E. Dombre, and P. Caron, "Hippocrate: An intrinsically safe robot for medical applications," in *Proc. 1998 IEEE/RSJ Intl. Conf. Intelligent Robots and Systems*, Victoria, Canada, Oct. 1998, pp. 959–964.
- [7] S. Boudet, J. Gariepy, and S. Mansour, "An integrated robotics and medical control device to quantify atheromatous plaques: Experiments on the arteries of a patient," in *IEEE Int. Conf. Intelligent Robotics and Systems*, vol. 3, 1997, pp. 1533–1538.
- [8] K. Baba, K. Satch, S. Satamoto, T. Okai, and I. Shiego, "Development of an ultrasonic system for three-dimensional reconstruction of the foetus," *J. Perinatal Medicine*, vol. 17, no. 1, pp. 19–24, 1989.
- [9] R. Ohbuchi, D. Chen, and H. Fuchs, "Incremental volume reconstruction and rendering for 3-D ultrasound imaging," *SPIE, Vis. Biomed. Comp.*, vol. 1808, pp. 312–323, 1992.
- [10] J. Sublett, B. Dempsey, and A. C. Weaver, "Design and implementation of a digital teleultrasound system for real-time remote diagnosis," in *IEEE Int. Conf. Computer-Based Medical Systems*, June 1995, pp. 292–299.
- [11] W. J. Chimiak, R. O. Rainer, N. T. Wolfman, and W. Covitz, "Architecture for a high-performance tele-ultrasound system," in *Medical Imaging: PACS Design and Evaluation: Engineering and Clinical Issues* Newport Beach, CA, 1996, vol. 2711, pp. 459–465.
- [12] A. Gourdon, P. Poignet, G. Poisson, P. Vieyres, and P. Marche, "A new robotic mechanism for medical application," in *IEEE/ASME Int. Conf. Advanced Intelligent Mechatronics*, 1999, pp. 33–38.
- [13] D. de Cunha, P. Gravez, C. Leroy, E. Maillard, J. Jouan, P. Varley, M. Jones, M. Halliwell, D. Hawkes, P. N. T. Wells, and L. Angelini, "The MIDSTEP system for ultrasound guided remote telesurgery," *IEEE Eng. Med. Biol. Mag.*, vol. 20, no. 3, pp. 1266–1269, 1998.
- [14] T. Umeda, A. Matani, O. Oshiro, and K. Chihara, "Tele-echo system: A real-time telemedicine system using medical ultrasound image sequence," *Telemedicine J.*, vol. 6, no. 1, pp. 63–67, 2000.
- [15] P. Abolmaesumi, S. P. DiMaio, S. E. Salcudean, R. Six, W. H. Zhu, and L. Filipozzi, "Teleoperated robot-assisted diagnostic ultrasound," in *Demo Presentation, IRIS/PREARN Conf.*, Montreal, 2000.
- [16] J. B. A. Maintz and M. A. Viergever, "A survey of medical image registration," *Med. Image Anal.*, vol. 2, no. 1, pp. 1–36, 1998.
- [17] L. Dong, G. Pelle, P. Brun, and M. Unser, "Model-based boundary detection in echocardiography using dynamic programming technique," in *SPIE Image Proc. Conf.*, vol. 1445, 1991, pp. 178–187.
- [18] T. Gustavsson, R. Abu-Gharbieh, G. Hamarneh, and Q. Liang, "Implementation and comparison of four different boundary detection algorithms for quantitative ultrasonic measurements of the human carotid artery," in *Proc. IEEE Comp. Cardiol.*, 1997, pp. 69–72.
- [19] T. Gustavsson, S. Molander, R. Pascher, Q. Liang, H. Broman, and K. Caidahl, "A model-based procedure for fully automated boundary detection and 3D reconstruction from 2D echocardiograms," in *Proc. IEEE Comp. Cardiol.*, Lund, Sweden, 1994, pp. 209–212.
- [20] R. Muzzolini, Y. Yang, and R. Pierson, "Multiresolution texture segmentation with application to diagnostic ultrasound images," *IEEE Trans. Med. Imag.*, vol. 12, pp. 108–123, Mar. 1996.
- [21] M. M. Choy and J. S. Jin, "Morphological image analysis of left-ventricular endocardial borders in 2d echocardiograms," in *SPIE*, vol. 2710, 1996, pp. 852–863.
- [22] A. Yezzi, S. Kichenassamy, A. Kumar, P. Olver, and A. Tannenbaum, "A geometric snake model for segmentation of medical imagery," *IEEE Trans. Med. Imag.*, vol. 16, pp. 199–209, June 1997.
- [23] M. Mignotte and J. Meunier, "Deformable template and distribution mixture-based data modeling for the endocardial contour tracking in an echocardiographic sequence," in *IEEE Int. Conf. Comp. Vis. Pat. Recog.*, vol. 1, 1999, pp. 225–230.
- [24] V. G. M. Paterni, M. Demi, A. Benassi, and V. Gemignani, "A real-time contour tracking system to investigate the cross-area sectional changes of the aorta," *Computers in Cardiology*, vol. 27, pp. 599–602, 2000.
- [25] J. G. Bosch, G. van Burken, S. S. Schukking, R. Wolff, A. J. van de Goor, and J. H. C. Reiber, "Real-time frame-to-frame automatic contour detection on echocardiograms," *Computers in Cardiology*, pp. 29–32, 1994.
- [26] V. Gemignani, M. Demi, M. Paterni, and A. Benassi, "Real-time implementation of a new contour tracking procedure in a multi-processor DSP system," *Circ. Sys. Commun. Comp.*, pp. 3521–3526, 2000.
- [27] P. Abolmaesumi, S. E. Salcudean, and W. H. Zhu, "Visual servoing for robot-assisted diagnostic ultrasound," in *World Congr. on Medical Physics and Biomedical Engineering*, vol. 4, Chicago, IL, July 2000, pp. 2532–2535.
- [28] P. Abolmaesumi, M. R. Sirouspour, and S. E. Salcudean, "Real-time extraction of carotid artery contours from ultrasound images," in *IEEE Symp. Computer-Based Medical Systems*, Texas, June 2000, pp. 181–186.
- [29] J. Dietrich, G. Plank, and H. Kraus, "Optoelectronic System Housed in Plastic Sphere," Eur. Patent 0 240 023; U.S. Patent 4 785 180; JP Patent 1 763 620.
- [30] W. H. Zhu, S. E. Salcudean, S. Bachman, and P. Abolmaesumi, "Motion/force/image control of a diagnostic ultrasound robot," in *IEEE Int. Conf. Robot. Auto.*, vol. 2, San Francisco, CA, 2000, pp. 1580–1585.
- [31] J. J. Mai, C. Kargel, S. Mhanna, and M. F. Insana, "Ultrasonic strain imaging in media with pulsatile flow," in *SPIE Medical Imaging Conf.*, vol. 4325, Feb. 2001.
- [32] L. G. Brown, "A survey of image registration techniques," *Computing Surveys*, vol. 24, no. 4, pp. 325–376, 1992.
- [33] N. Friedland and D. Adam, "Automatic ventricular cavity boundary detection from sequential ultrasound images using simulated annealing," *IEEE Trans. Med. Imag.*, vol. 8, no. 4, pp. 344–353, Dec. 1989.
- [34] Y. Bar-Shalom and T. E. Fortmann, *Tracking and Data Association*. New York: Academic, 1988.
- [35] C. M. Chen, H. H. S. Lu, and Y. C. Lin, "A new ultrasound image segmentation algorithm based on an early vision model and discrete snake model," in *SPIE*, vol. 3338, 1998, pp. 959–970.
- [36] S. Hutchinson, G. Hager, and P. I. Corke, "A tutorial on visual servo control," *IEEE Trans. Robot. Automat.*, vol. 12, pp. 651–670, Oct. 1996.
- [37] R. W. Prager, R. N. Rohling, A. H. Gee, and L. Berman, "Automatic calibration for 3-D free-hand ultrasound," Dep. Eng., Cambridge Univ., CUED/F-INFENG/TR 303, 1997.
- [38] A. H. Gee and R. W. Prager, "Sequential 3D diagnostic ultrasound using the Stradx system," in *Medical Image Computing and Computer Assisted Intervention*, C. Taylor and A. Colchester, Eds. New York: Springer, 1999, pp. 716–725.
- [39] S. E. Salcudean and N. R. Parker, "6-DOF desk-top voice-coil joystick," in *6th Symp. Haptic Int. Virtual Env. Teleoper. Sys.*, vol. 61, Dallas, TX, Nov. 16–21, 1997, pp. 131–138.



Purang Abolmaesumi (S'99) was born in Tehran, Iran, in 1973. He received the B.Sc. and M.S. degrees in electrical engineering from Sharif University of Technology, Tehran, Iran, in 1995 and 1997, respectively. Since January 1998, he has joined the Robotics and Control Laboratory at the University of British Columbia, Vancouver, Canada, where he is pursuing a doctoral degree in Electrical and Computer Engineering.

His research interests include medical robotics, medical ultrasound image processing, computer vision, tele-robotics, haptics, image guided robots, and 3-D medical imaging.



Septimiu E. Salcudean (M'74) received the B. Eng. and M.Eng. degrees from McGill University, Montreal, Canada, and the Ph.D. degree from the University of California at Berkeley, all in electrical engineering.

From 1986 to 1989, he was a Research Staff Member in the robotics group at the IBM T.J. Watson Research Center. He then joined the Department of Electrical and Computer Engineering at the University of British Columbia, Vancouver, Canada, where he is now a Professor and holds a

Canada Research Chair. He spent one year at ONERA in Toulouse, France, in 1996-1997, where he held a Killam Research Fellowship. Dr. Salcudean is interested in haptic interfaces, teleoperation and virtual environments. He is pursuing applications to medical diagnosis and intervention and to the control of heavy-duty hydraulic machines such as excavators.



Mohammad Reza Sirouspour (S'00) was born in Tehran, Iran, in 1973. He received the B.Sc. and M.S. degrees in electrical engineering from Sharif University of Technology, Tehran, Iran, in 1995 and 1997, respectively.

During 1996-1998 he was a research engineer at the Sharif Electronic Research Center, Tehran, Iran. Since September 1998, he has joined the Robotics and Control Laboratory at the University of British Columbia, Vancouver, Canada, where he is pursuing a doctoral degree in Electrical and Computer Engineering.

His research interests include control of robot manipulators, nonlinear control, tele-robotics, haptics, and estimation theory.



Wen-Hong Zhu (M'97) received the Bachelor's and M.S. degree from Northwestern Polytechnic University, Xi'an, China, in 1984 and 1987, respectively, both in aeronautical control engineering, and the Ph.D. degree in information and control engineering from Xi'an Jiaotong University, Xi'an, China, in 1991.

He was employed by the CIET, KAIST, Korea, as a Postdoctoral Fellow in 1995. From 1996 to 1997, he was awarded a Postdoctoral Fellowship by the Katholieke Universiteit Leuven, Belgium. He

worked with Prof. Tim Salcudean at University of British Columbia (UBC) as a Postdoctoral Fellow from December 1997 to March 1999, and as a Research Engineer from April 1999 to January 2001. He is now with the Canadian Space Agency, St-Hubert, Canada. His research interests include stability guaranteed teleoperation, teleoperated control of medical robots, virtual decomposition control of multiple-closed-chain robotic systems, adaptive control of space robots, adaptive control of robots with rigid/flexible joints, coordinated control of multi-arm robots, variable structure control of robots with joint position measurements, and application of robots in service fields.



Simon P. DiMaio (S'97) received the B.Sc. degree in electrical engineering from the University of Cape Town, South Africa, in 1995. In 1998 he completed the M.A.Sc. degree at the University of British Columbia, Canada, where he is currently working toward the Ph.D. degree in electrical engineering.

His research interests include the control of robotic mechanisms, environment model identification, virtual environment simulation, medical simulation, and haptics.